KOH wet etching mechanisms of III–N nanopillars: Impact of temperature and concentration

Jaloustre Lucas, Sales de Mello Saron-Rosy, Labau Sébastien, Petit-Etienne Camille, Pargon Erwine

KOH wet etching mechanisms of III-N nano-pillars: Impact of temperature and concentration

Jaloustre Lucas [a], Sales De Mello Saron-Rosy [a], Labau Sébastien [a], Petit-Etienne Camille [a], Pargon Erwine [a]*

[a] Univ. Grenoble Alpes, CNRS, CEA/LETI-Minatec, Grenoble INP, Institute of Engineering and Management University Grenoble Alpes, LTM, Grenoble F-38054, France

KEYWORDS: AlN; GaN; KOH wet etching; Crystal orientation dependent process; roughness formation

ABSTRACT: Combining dry and wet etching processes is a common technique to pattern III-N semiconductors integrated in optoelectronics devices with a controlled final shape and high-quality crystallographic facets. However, the wet mechanisms driving the final pattern morphology have never been deeply studied. In this article, we investigate the mechanisms involved during KOH wet etching applied on AlN and GaN pillars previously obtained by Cl_2 plasma etching with hexagonal hard mask, whose edges are oriented either with *a*- or *m*-nonpolar III-N crystallographic orientation. These pillars are intended to serve as the first building blocks for core-shell Ultraviolet light emitting diodes (UV LED), for which the quality of the patterning of the III-N core pillar plays a key role in the subsequent quantum well regrowth. We discuss the impact of the KOH concentration (5 wt% vs 44 wt%) and the solution temperature (from room temperature to 80°C), and of the hard mask orientation on the etching kinetics, the etch propagation mechanisms, the crystallographic plane stability and the

roughness formation. Our results show how the stability of the *c* and *m* crystallographic planes and the vulnerability of specific kinks sites determine the progression of the KOH wet etching process and the formation of roughness depending on the wet etching conditions and the shape of the hard mask used. With this understanding, we developed a two-step process combining dry and wet etching capable of fabricating high aspect ratio AlN and GaN nanopillars with the desired smooth and anisotropic *m*-oriented sidewalls.

INTRODUCTION: Nitride semiconductor (III-N, such as AlN, GaN and their alloys) are widely used in optoelectronic applications that take advantage of their wide bandgap and unique properties.[1,2] A key requirement for application of III-N semiconductors is the development of advanced wet and dry etching techniques for patterning of device structures with a controlled final shape and specific crystallographic facets.

Recently, III-N semiconductors have attracted significant interest to serve as building blocks for eco-friendly energy-efficient UV sources in a core-shell architecture.[3,4] Such applications involve the fabrication of well-organized arrays of high aspect ratio AlN or GaN nanowires (the core) upon which the UV emissive quantum wells (the shell) are radially grown. After the patterning step, III-N nanowires with smooth, anisotropic, and *m*-faceted sidewalls are highly desired to ensure high-quality quantum well regrowth.

Cl_2-based plasmas are often recognized as the most suitable plasma chemistry to pattern III-N semiconductors via a top-down approach. They allow anisotropic transfer, with quite reasonable etch rate (200-500 nm/min)[5–7] as well as minimal surface defects and roughness when compared to plasmas with BCl_3 or $SiCl_4$ additives.[8–10] Another interesting aspect of chlorine-based plasmas for III-N etching is that, for some peculiar plasma conditions, they can lead to a preferential crystallographic orientation dependent etching effect, revealing facets with *a*-crystallographic orientation.[11] In recent publications, we discussed the etching mechanisms of GaN and AlN in Cl_2 plasma.[11,12]

Wet etching offers an alternative approach to patterning III-N semiconductors, either used alone or as a complement to plasma-based processes. Combining dry and wet etching processes allows leveraging the advantages of both approaches to achieve high-quality, anisotropic structures.[13–15] Dry etching is used to define the initial pattern with controlled geometries. A subsequent wet etching step refines and straightens the sidewalls, removing plasma-induced damage and might reveal crystallographically stable facets.[15,16] This hybrid approach provides a pathway for fabricating advanced III-N structures, with the precision of plasma etching and the surface quality enhancement of wet etching, as demonstrated in our previous work targeting the fabrication of high aspect ratio III-N nanowires with *m*-facetted sidewalls.[12,17]

Most of the work related to the wet etching of III-N semiconductors relies on the use of aqueous alkaline solutions such as KOH, NaOH, TMAH, and AZ400K (a KOH-based resist developer). There are many reports in the literature demonstrating the effectiveness of OH^- based solutions, at room temperature or heated, to structure III-N pattern (especially for GaN, fewer studies on AlN).[15,18–30] However, only a few works address the etching mechanisms that can be involved. It has been published that the etching mechanism of GaN (or AlN) in OH-based solution relies on the oxidation of metallic atoms (Al or Ga) through hydroxide (OH^-) molecules, which attack and break the metal–N bonds, freeing the metallic atom, which is subsequently oxidized (Ga_2O_3 or Al_2O_3) and dissolved in the solution.[23,26,31] Lai's work,[26] established a parameter named the Etching Barrier Index (EBI) to evaluate the etching potential of the different crystallographic planes of III-N under KOH. This quantity is defined as the number of dangling bonds per nitrogen atom on a plane multiplied by the planar atomic density of this plane. A high EBI indicates a high density of negatively charged nitrogen atoms able to repel the OH^- ions, reducing the probability for these ions to attack the III-N bond and to bond with Ga (or Al) atoms. In other words, crystallographic planes with a high EBI are chemically

more stable. According to the EBI values of GaN and AlN[12,24,26] the plane stability in III-N varies as follows:

$$c\text{-plane} \gg m\text{-nonpolar} > a\text{-nonpolar} \gg \text{semipolar} \quad (1)$$

This trend indicates that the *c*-plane is the most stable under KOH etching, while semi-polar planes, exhibit the lowest stability.

In the present article, we propose to give new insights on the mechanisms involved in the KOH wet etching of AlN and GaN semiconductors. For this purpose, we investigate the KOH wet etching of AlN and GaN pillars previously obtained by Cl_2 plasma etching with hexagonal SiO_2 hard mask.

We show and discuss the impact of the KOH concentration (5 wt% vs 44 wt%) and the solution temperature (from room temperature to 80°C) on the etching kinetics, the etch propagation mechanisms, the crystallographic plane stability, and the roughness formation. Based on our findings, we propose in the conclusion the best options to pattern high aspect ratio AlN and GaN nanowires with smooth and *m*-oriented facets by using a hybrid approach combining dry and wet etching steps.

EXPERIMENTAL METHODS:

The experimental methods follow that described in our previous work[12].

SAMPLE PREPARATION:

Micro-pillar fabrication was carried out on commercially available wafers of unintentionally doped III-N (AlN or GaN) of 4-µm thickness, with a metal polarity (0001), grown on c-sapphire, and provided by Nanowin company. A 1400 nm thick SiO_2 (resp. 850 nm) HM layer was deposited on the AlN (resp. GaN) layer using Plasma Enhanced Chemical Vapor Deposition (PECVD) with tetraethoxysilane (TEOS) at 480 °C in a DxZ CVD reactor from Applied Materials. The wafer was then diced into coupons of 7 by 11 mm.

For the patterning, an electron-sensitive resist (ma-N 2410) was then spin-coated on the samples and insolate using electron beam lithography. The patterns consisted of dots with hexagonal shapes and diameters (inscribed circles) varying from 0.25 µm to 2 µm. The hexagonal dots had two orientations corresponding to *a*-planes {11-20} and *m*-planes {1-100} of AlN (or GaN), with a precision on the dot's alignments of ±2°. More details about the samples are available in our previous works.[11,12,17] The III-N unit cell, along with the orientation of the *c*-, *a*-, and *m*-planes, is shown in Figure 1.

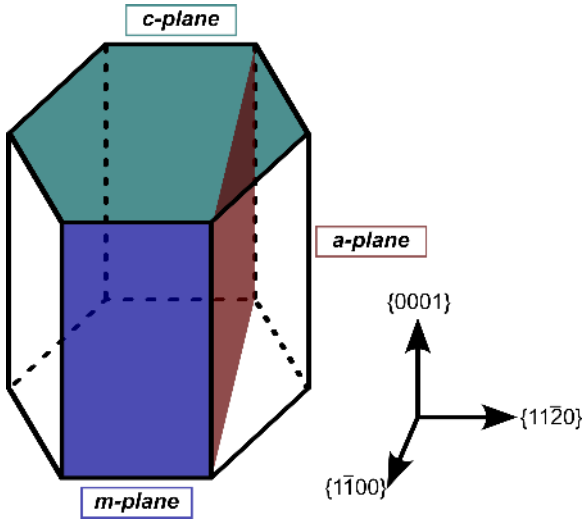

Figure 1. Wurtzite unit cell of III-N showing the orientations of the *c*-, *a*-, and *m*-planes, along with their corresponding (hkil) Miller-Bravais indices.

PLASMA ETCHING:

Centura 5200 etch platform from Applied Materials, which consists of three plasma reactors designed for 200 mm wafers. Etching followed a similar multistep plasma process as in our previous work[12], involving Magnetically Enhanced Reactive Ion Etching MERIE reactor, $Ar/C_4F_8/O_2$ plasma, and a Si carrier wafer (CW) for the hard mask opening step, while an Inductively Coupled Plasma (ICP) reactor, Cl_2 plasma, and a Si_3N_4 CW are used for the AlN/GaN etching.

The plasma etching of GaN and AlN pillars was already optimized in our previous works.[11,12] We highlighted in these articles that tapered profiles after plasma etching were required for an efficient anisotropic etching during the subsequent KOH wet step.

For GaN, we used plasma parameters leading to the formation of slightly tapered pillars (around 1.2°).[11] For AlN, the selected plasma parameters produced strongly tapered pillars (around 5.2°).[12] These parameters are given in Table 1. In both cases, the bias power was adjusted to achieve a direct current self-bias voltage (V_{DC}) of -460 V, while the chuck temperature was maintained at 55 °C.

Table1. Plasma parameters used for the GaN and AlN etching.

	Cl_2 (sccm)	Source power (W)	Bias power (W)	Pressure (mTorr)	Time (s)
GaN	190	400	150	20	1400
AlN	160	400	220	10	1230

The difference in profile (slightly tapered for GaN and strongly tapered for AlN) is driven by the wet etching rates of the III-N. Indeed, AlN is etched 100 times faster than GaN in 44 wt% KOH.[12,16,19] So slightly tapered profiles are preferred for GaN to avoid excessively long etching durations, while strongly tapered profiles for AlN allow better observation and understanding of the wet etching process.

WET ETCHING:

The wet etching experiments were performed in a chemical fume hood located within a clean room, with the temperature maintained at 20 °C. KOH wet etching of GaN and AlN were performed using a KOH solution with a weight concentration of 44 wt% provided by CMC Materials. The same solution was diluted in deionized water to obtain a 5 wt% KOH. The impact of temperature on KOH wet etching mechanisms was also investigated using heated solutions with several KOH dilutions. These experiments were conducted in a different chemical bench, where the maximum KOH concentration available was 40 wt%. The

temperature and dilution range investigated were from 40°C to 80°C ±2°C, and from 1 wt% to 40 wt% rescpectively. The temperature control was achieved using a hot plate, monitored and regulated by a thermometer. Due to the presence of the thermometer, the beaker containing the KOH solution was left uncovered, leading to the gradual evaporation of the solution over time. Titration experiments were conducted and revealed that the OH^- concentration is increased of about 2 wt% after heating the KOH solution (cf. Table S1).

When needed, 1 wt% hydrofluoric acid (HF) solution diluted in water during 60s was used to remove the Si-based passivation layer formed on the pillar sidewalls during the plasma etching. Finally, the removal of the SiO_2 HM was performed (before or after the KOH wet treatment) using a 50 wt% HF solution diluted in water during 60s. For all previously mentioned wet treatments, the samples were submerged into the solution without any agitation. Following the wet treatments, the samples were rinsed in deionized water for 2 minutes and dried using a nitrogen (N_2) flow.

CHARACTERISATIONS:

A FEI Helios-450s Focused Ion Beam Scanning Transmission Electron Microscopy (FIB-STEM) system was used to acquire the SEM images of the pillars after the different steps of dry and wet etching. To ensure uniform grayscale and enhance contrast across images, all SEM images underwent post-processing using a contrast-limited adaptive histogram equalization (CLAHE) algorithm from the Python OpenCV library.

A Bruker Dimension Icon atomic force microscope (AFM) was used in tapping mode and with OTESPA-R3 probes to characterize the sidewall roughness of the pillars. The AFM images were captured on 2 µm-diameter fallen pillars that were manually broken using a needle. The analyzed pillars are selected randomly among the pillars present and fallen in the sample area dedicated to 2 µm diameter. The broken pillars were then glued to the sapphire substrate at both

their top and bottom parts through a localized platinum deposition, carried out using a FIB (cf. Figure 2a). This procedure ensured strong adhesion of the pillars, guaranteeing that they remained stable and did not shift during AFM observations. However, the limited number of scanned areas and the inherent AFM constraints (tip convolution, limited scan size) impact the accuracy and representativity of surface characterization. As a result, AFM measurements may highlight local features that are not fully representative of the entire sample, only allowing for the observation of trends. From the AFM images, we extracted the root mean square (RMS) roughness of the pillar's sidewalls. This was done using two different methods:

i) A "global" RMS roughness is computed on the entire sidewall. To do this, a 1x3 µm region was cropped from the AFM images. This area size maximized the sidewall representation while ensuring that no edges were included in the analysis (cf. Figure 2b).

ii) On the same area, a "local" RMS roughness was calculated using a 250x250 nm box. This box was slid across the entire 1x3 µm region, allowing to calculate the roughness at each point along the sliding path. The result was a detailed roughness map of the entire 1x3 µm area, the 'local' roughness corresponds to the median roughness value of this roughness map (cf. Figure 2c).

This choice of analysis allows comparing pillar sidewalls overall quality using the "*global*" roughness, which is mostly sensitive to important topographic variations. The "*local*" roughness is more sensitive to finer surface variations and irregularities. This combined approach offers both a large-scale and a fine understanding of the material's texture.

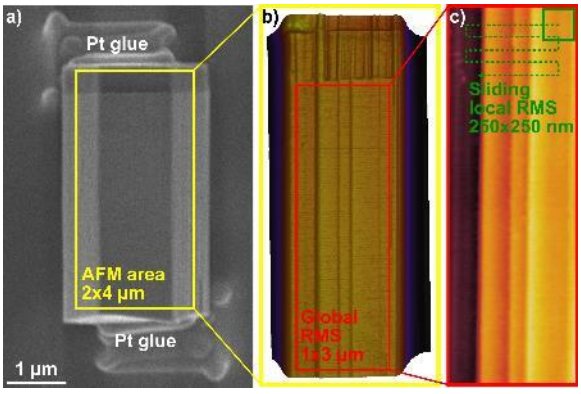

Figure 2. a) SEM image of a fallen 2 µm diameter pillar glued with Pt at the top and bottom, AFM analysis was performed on the yellow area. b) Raw AFM image of the pillar, the global roughness is extracted from the red area. c) AFM image of the red area after flattening, local roughness corresponds to the mean roughness of the 250x250 nm green box, moved across the image.

RESULTS:

IMPACT OF THE KOH CONCENTRATION ON III-N PILLAR ETCHING:

Figure 3 shows the behavior of AlN pillars under two different KOH wet treatments (44 wt% and 5 wt%) at room temperature for different durations. The SiO_2 hard mask used during the plasma etching step is kept for the wet etching. This allows the HM shape to be anisotropically transferred into the tapered pillars without generating damage at the pillar's top edges, as detailed in our previous works.[12,17]

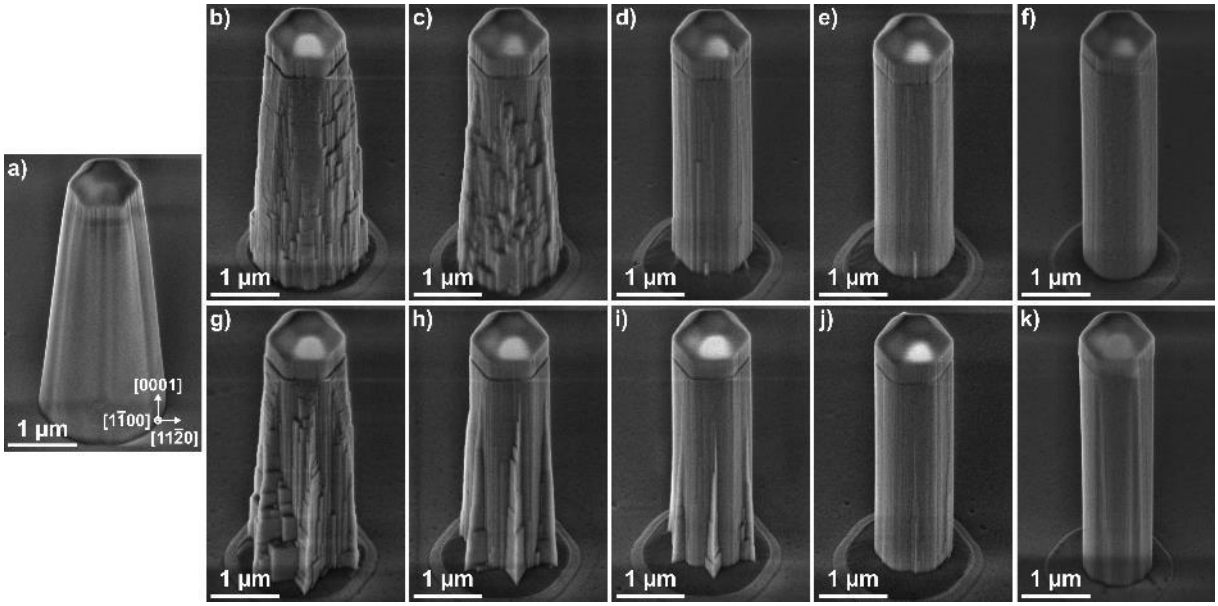

Figure 3. SEM images of AlN pillars of 1 µm diameter with *m*-oriented HM after a) plasma etching, b-f) 44 wt% KOH wet treatment during: 20, 60, 180, 360, and 4800 seconds respectively. g-k) 5 wt% KOH wet treatment during: 2, 6, 10, 20, and 120 minutes respectively.

With a KOH concentration of 44 wt% (Figure 3b to Figure 3f), the etching of the tapered sidewalls not protected by the hard mask is achieved quickly, with a full HM transfer in less than 360 seconds, resulting in straight pillars (Figure 3e). During this process, the wet etching propagates by forming a staircase-like pattern around the pillar.

With a KOH concentration of 5 wt% (Figure 3g to Figure 3k), the etching of the tapered sidewalls is at least more than three times slower, taking around 20 minutes to complete. As with 44 wt% KOH, the end result is a perfectly straight pillar (Figure 3j). However, at this lower KOH concentration, the wet etching progression is noticeably different. As shown in Figure 3g star-like pattern composed of six branches appears on the tapered area before the complete straightening of the pillar.

Further investigations have been done to uncover the etching mechanisms responsible for these differing behaviors. Figure 4 shows the same experiment, performed with a short KOH duration (20 seconds for the 44 wt% KOH and 2 minutes for the 5 wt% KOH) but this time on pillars without HM.

From this experiment, we can measure the AlN etching rates for both wet treatments. For 44 wt% KOH the vertical etching progresses at roughly 1 to 1.5 µm per minute (Figure 4a), which is coherent with a near-complete etching of the tapered sidewalls in 4 minutes. Since no HM is present to protect the pillar tops, lateral erosion is also present and occurs at around 60 nm/min, meaning that 500 nm diameter pillars are fully consumed in roughly 5 minutes.

In contrast, the etching with 5 wt% KOH is not homogeneous due to the formation of branches. Between the branches, the vertical consumption is extremely fast in contrast, the vertical etch rate at the branch locations is significantly slower, around 200 nm/min, explaining the 20 minutes required to fully straighten the pillars. Lateral etching at the pillar tops is also present, at a rate of around 10 nm/min.

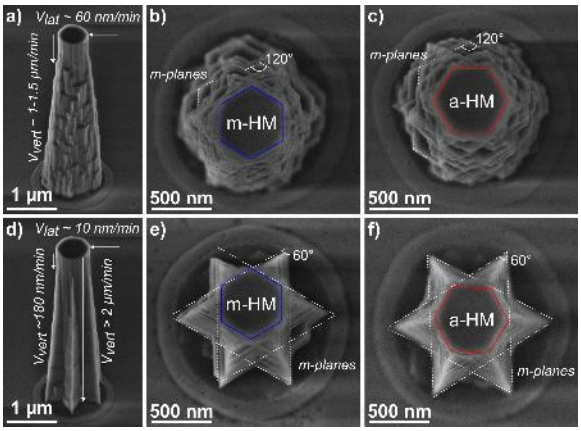

Figure 4. SEM images of 500 nm diameter AlN pillars in tilt and top view after: a-c) 44 wt% KOH treatment during 20 sec. d-f) 5 wt% KOH treatment during 2 min. In the top view images, the *m*-plane of AlN is marked with dashed lines, and the initial HM shape (*a*- or *m*-) prior to the 50 wt% HF removal is indicated.

Top view images of the pillars (Figure 4b and Figure 4c for 44 wt% KOH, and Figure 4e and Figure 4f for 5 wt% KOH) reveal several key information. First, the initial HM shape does not affect the etching of the tapered sidewalls; only the KOH concentration plays a role, as indicated by the similar profiles for both *a*- and *m*-oriented HM (see Figure 4b, Figure 4e, and Figure 4c, Figure 4f). Then, both KOH concentrations reveal vertical *m*-planes, indicated by dashed lines in Figure 4b, 4c, 4e, and 4f as well as horizontal *c*-terraces, which is consistent with the EBI model described in Equation 1. However, with 44 wt% KOH, the *m*-planes form obtuse angles of 120° between adjacent *m*-planes (Figure 4b and Figure 4c). In contrast, with 5 wt% KOH, adjacent *m*-planes form acute angles of 60° (Figure 4e and Figure 4f), resulting in a star-like shape. The mechanisms driving this differing behavior will be discussed in section 4.

Similar KOH experiments on GaN pillars were performed, the end results being compared to the AlN ones in Figure 5.

The wet etching of GaN is significantly slower than that of AlN, requiring approximately 10 hours with 44 wt% KOH and around 28 hours with 5 wt% KOH to reach straight pillars (see Figure 5e to Figure 5h). For both concentrations, the wet etching progresses with the formation

of staircase-like roughness on the pillar sidewalls (not shown here), similar to the effect observed with 44 wt% KOH on AlN (cf. Figure 5a and Figure 5b). No star-like shapes were observed.

Finally, after the complete wet transfer using *a* or *m*-oriented HM, AlN and GaN show very similar anisotropic profiles. The final profile does not depend on the KOH concentration but on the HM shape. Whatever the KOH concentrations used, the wet etching transfers either the *m*- or *a*-oriented hexagon. However, the *m*-oriented facets are smooth whereas the *a*-facets are rough with numerous vertical striations (cf. Figure 5).

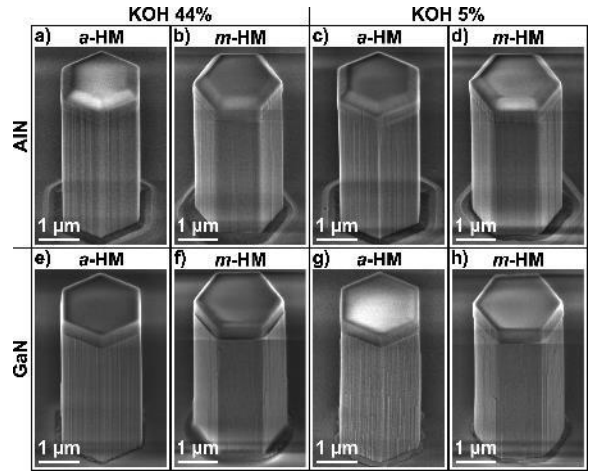

Figure 5. SEM images of 2µm diameter III-N pillars with *a*- and *m*- oriented HM after plasma etching and wet treatment: a-b, c-d) AlN treated with 44 wt% KOH and 5 wt% KOH during 10 min and 50 min, respectively. e-f, g-h) GaN treated with 44 wt% KOH and 5 wt% KOH, during 10 hours and 28 hours respectively.

Once the pillars are fully anisotropic, extended KOH treatment does not lead to further lateral etching of the pillars, confirming the stability of the revealed vertical nonpolar planes (cf. Figure 3f showing an overetch of more than 1000%, and Figure 3k an overetch of 500%). However, for AlN pillars exposed to prolonged 5 wt% KOH it is noticed that the intersection between two vertical planes starts to be consumed (cf. Figure 3k). This will be discussed in Section 4.2.

IMPACT OF THE KOH CONCENTRATION ON III-N PILLAR SIDEWALLS ROUGHNESS:

A more in-depth study of the impact of the KOH concentration and the HM orientation on the pillar sidewalls roughness has been conducted using AFM on fallen pillars of 2 µm diameters. Figure 6 shows the AFM images of AlN and GaN pillar sidewalls treated with both 44 wt% and 5 wt% KOH, with *a*-oriented and *m*-oriented HM. From these topographic images, a 'global' and a 'local' RMS roughness of the sidewalls can be extracted (cf. Figure 7). Details of the AFM protocol and data treatment are available in section 2.4.

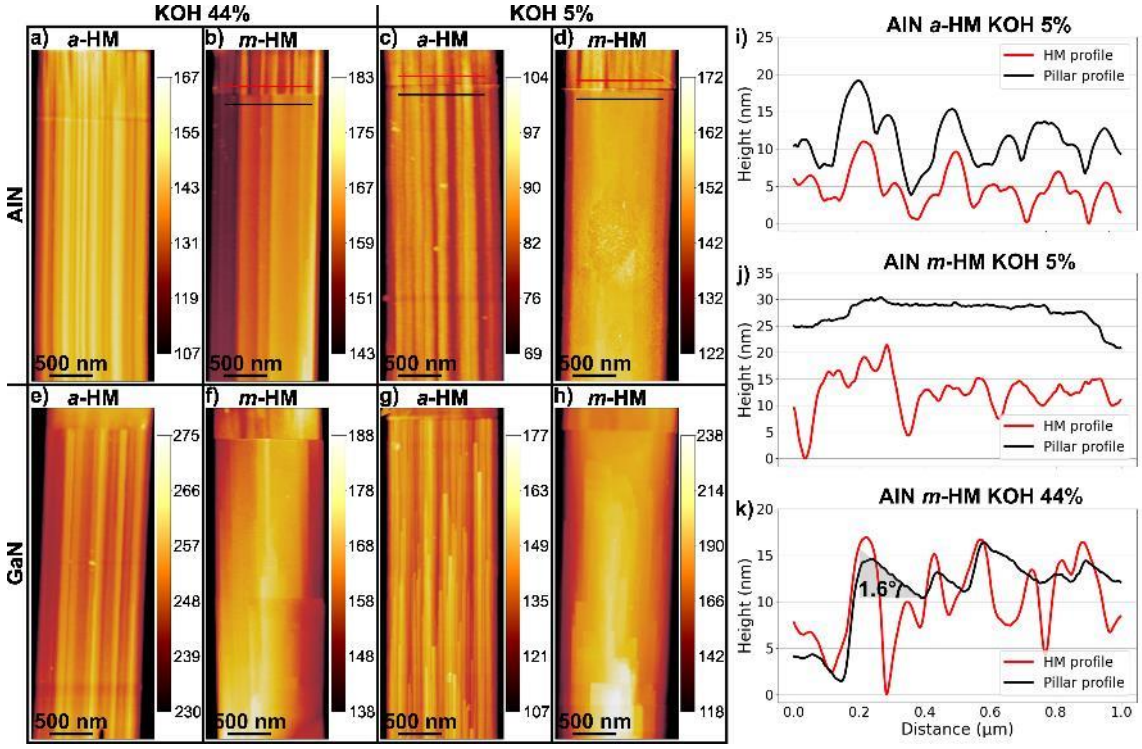

Figure 6. AFM images of AlN and GaN pillars after KOH wet treatment: a-b) 44 wt% KOH on *a*- and *m*-oriented AlN pillars. c-d) 5 wt% KOH on *a*- and *m*-oriented AlN pillars. e-f) 44 wt% KOH on *a*- and *m*-oriented GaN pillars. g-h) 5 wt% KOH on *a*- and *m*-oriented GaN pillars. i-k) Linecut performed on the HM and the AlN pillar treated with 5 wt% or 44 wt% KOH for *a*- and *m*-oriented HM. Linecut positions are represented by the bold lines on images b), c), and d).

AFM on AlN pillars (Figure 6a to Figure 6d):

AlN pillars with *a*-oriented HM treated with 44 wt% or 5 wt% KOH (Figure 6a and Figure 6c) exhibit numerous vertical striations that begin at the top of the pillars and extend down to the bottom. These striations originate from the HM, which is striated after the plasma etching process. They are transferred to the pillar sidewalls during the wet etching as highlighted by the linecuts of Figure 6i. The presence of these striations on the pillar's sidewalls results in a local roughness of 2.1- 2.2 nm and a global roughness of 3-4 nm (cf. Figure 7), similar to the HM roughness value, which is around 3.5 ±1 nm.

AlN pillars with *m*-oriented HM treated with 44 wt% or 5 wt% KOH (Figure 6b and Figure 6d) show no or few striations compared to those with *a*-oriented HM. Figure 6j confirms that the pillar's sidewalls roughness does not follow the HM roughness profile. This result in a relatively smooth sidewall, mostly composed of a single *m*-plane. Consequently, the local roughness is lower with *m*-oriented HM (0.9-1.1 nm) than with *a*-oriented HM (2.1-2.2 nm) (cf. Figure 7). In contrast, the global roughness is relatively high (3 to 5 nm), especially for 44 wt% KOH. In this case, the global roughness is not attributed to HM striation transfer but rather to jumps from one *m*-plane to another. We suspect that those jumps are caused by a slight misalignment of +/- 2° between the HM edges and the AlN *m*-plane that originates from the manual positioning of the sample during the lithography step. This is confirmed by the linecut shown in Figure 6k, which reveals that the *m*-plane is slightly tilted (1.6°) relative to the HM. The highest global roughness obtained at 44 wt% will be discussed in section 4.2.

AFM on GaN pillars (Figure 6e to Figure 6h):

GaN pillars mostly behave like AlN ones. For both KOH concentrations, pillars with *a*-oriented HM exhibit numerous vertical striations (see Figure 6e and Figure 6g), while pillars with *m*-oriented HM show no striations, but instead exhibit staircase-like roughness composed

of parallel *m*-planes (see Figure 6f and Figure 6h). Consequently, the local roughness (see Figure 7) is lower with *m*-oriented HM (0.7-1.2 nm) than with *a*-oriented HM (2.2-3.8 nm).

For 5 wt% KOH, the global and local roughness values are much higher than the ones obtained for 44 wt% KOH (for both *a*- and *m*- orientations). This tendency is attributed to the extended etching duration (28 h) needed at this concentration to get anisotropic GaN pillars. Over such a long period, the erosion of the SiO_2 HM by the KOH solution becomes significant.[17,32] As the HM diameter decreases, the vulnerable top edges of the pillars are progressively exposed to KOH, resulting in a continuous lateral and vertical etching of the pillar sidewalls. This process perpetually generates new striations or staircase roughness on *a*- and *m*-oriented pillars, resulting in significantly rougher sidewalls (line cuts on GaN pillars are shown in Figure S2).

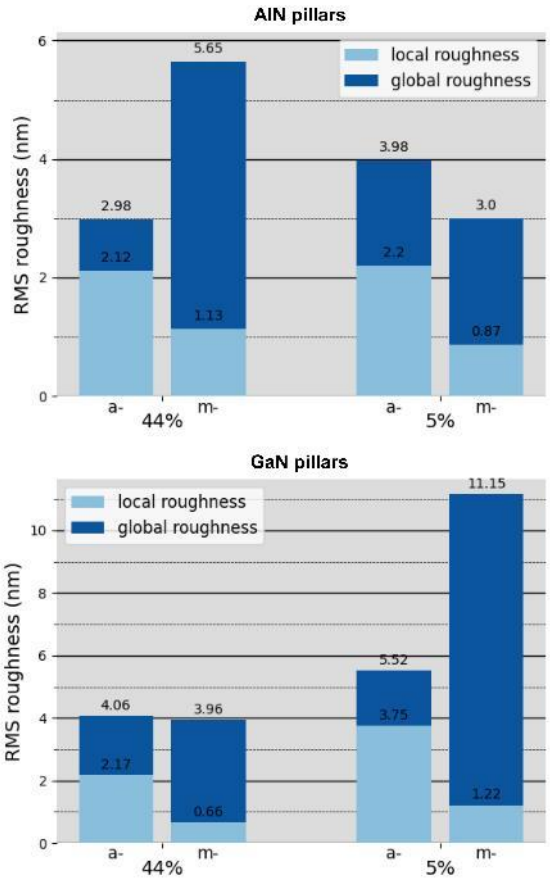

Figure 7. Box plot of the local and global RMS roughness for AlN pillars (top) and GaN pillars (bottom), with *a*- and *m*-oriented HM, and treated with 44 wt% and 5 wt% KOH.

IMPACT OF THE TEMPERATURE IN THE WET ETCHING:

Another important parameter investigated was the impact of the temperature on the etching of GaN and AlN with KOH. As previously demonstrated, the HM transfer onto the pillars requires significant time, around 50 minutes for AlN etched with 5 wt% KOH and up to 10 hours for GaN etched with 44 wt% KOH. Such long process times are not ideal, and increasing the etching kinetics could be highly beneficial. To shorten the wet etching time, the utilization of heated KOH was tested at various temperatures ranging from 40°C to 80°C for two dilutions 5 wt% and to 40 wt%. Note that during the heating experiments, the OH^- concentration may vary and increase of 2 wt% maximum in the temperature range investigated in this study (cf. Table S1).

Figure 8a and Figure 8b shows GaN pillars etched with 40 wt% KOH heated at 60°C. At this temperature, GaN pillars can be straightened in approximately 6 minutes, which represents a significant reduction compared to the 10 hours previously required. Similarly, Figure 8c and Figure 8d shows AlN pillars etched with 5 wt% KOH heated at 60°C. Here, straightening occurs in 40 seconds instead of the 50 minutes required at 5 wt% room temperature. In both cases, heating the KOH solution at 60°C reduces the etching time by two orders of magnitude, making this wet etching process much more efficient and practical.

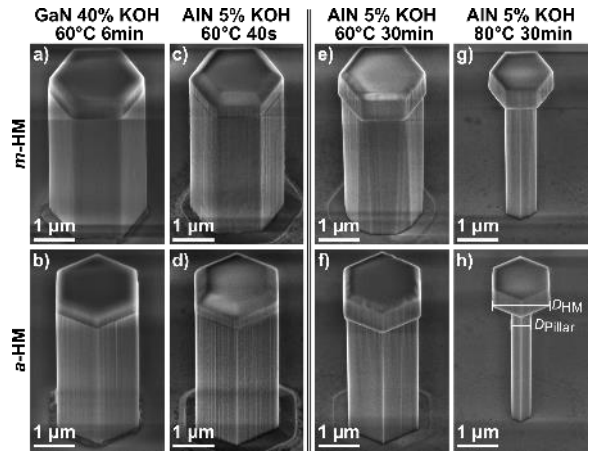

Figure 8. SEM images of 2 µm-diameter pillars with *m*- and *a*-oriented HM (top and bottom). a, b) GaN pillars etched with 40 wt% KOH at 60°C during 6 minutes. c, d) AlN pillars etched

with 5 wt% KOH at 60°C during 40 seconds. e-h) AlN pillars etched with 5 wt% KOH during 30 minutes at 60°C and 80°C.

Similarly to room temperature experiments, we observe that smooth sidewalls are obtained with *m*-oriented HM while *a*-HM leads to the formation of rough and striated sidewalls. Additionally, we observe that the wet etch of AlN in 5 wt% (40 wt% resp.) heated KOH progresses with star-like (staircase resp.) patterns.

However, unlike room temperature KOH, we also notice that AlN pillars exposed to heated KOH for extended periods begin to exhibit lateral etching, even with the HM still in place (see Figure 8e to Figure 8h at 60°C or 80°C solution temperature). This behavior suggests that the nonpolar planes forming the sidewalls become vulnerable when the KOH solution is hot enough, as observed in previous studies.[30,33,34]

By measuring the diameter of the *a*-oriented HM and the pillar after prolonged exposure to heated KOH (illustrated in Figure 8h), the etching rates of the SiO_2 HM and the AlN nonpolar plane were determined as a function of KOH temperature and concentration. These rates correspond to the etching of a single side, derived as half the measured diameter reduction. Note that to ensure that we only measure the etching rate of the non-polar planes, this experiment have been performed on pillars already straightened using 44 wt% KOH at room temperature for 10 minutes (as shown in Figure 5a and Figure 5b). The results, presented in Figure 9, show that the etching rates of SiO_2 and AlN increase exponentially with temperature for both KOH concentrations, following an Arrhenius law (cf. Equation 2).

$$ER = A \cdot e^{-\frac{E_a}{RT}} \quad (2)$$

Where ER is the etch rate of the reaction in nm/min, A is the pre-exponential factor, E_a is the activation energy in kJ/mol, R is the universal gas constant (8.314 $J.K^{-1}.mol^{-1}$), and T is the absolute temperature in Kelvin.

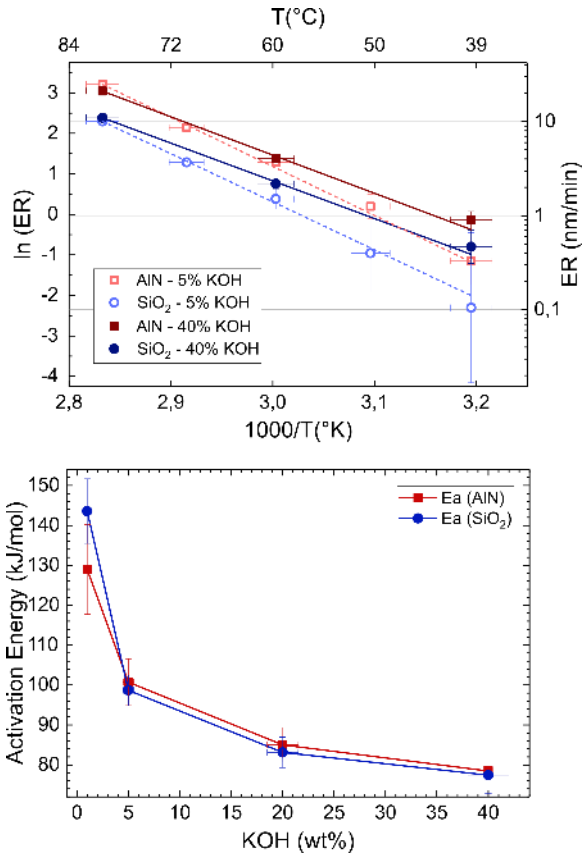

Figure 9. Top: Etching rates of SiO_2 HM and AlN nonpolar sidewalls (measured on *a*-oriented pillars, as shown in Figure 8h) versus temperature of the 5 wt% and 40 wt% KOH solution, the lines represent the Arrhenius fit. Bottom: Activation energy of SiO_2 and AlN as a function of KOH concentrations. These values are extracted from the Arrhenius fit. Etching rates obtained for all KOH concentrations are available in Figure S3.

For all KOH concentrations (cf. Figure 9 and Figure S3), the SiO_2 etch rate is lower than the AlN nonpolar plane one. For both materials, high KOH concentrations result in higher etch rates at low temperatures. However, as the temperature increases, this difference is reduced, and etch rates become comparable for high and low KOH concentrations. This transition occurs at 70°C for AlN and 80°C for SiO_2, beyond which lower KOH concentrations are expected to yield higher etch rates.

The AlN/SiO_2 etch selectivity is 2.5 at 5 wt% KOH vs 1.9 at 40 wt% KOH and does not depend on the temperature. Indeed, AlN and SiO_2 exhibit very similar activation energy values,

meaning that their etching rates and thus AlN/SiO_2 etch selectivity evolve similarly with temperature. At low KOH concentration (1 wt%), the activation energies of SiO_2 and AlN are 143.6 kJ/mol and 129 kJ/mol, respectively. As the KOH concentration increases, the activation energy decreases significantly up to 20 wt% KOH. Beyond this point, the decrease slows down, and the activation energy gradually stabilizes, reaching 77.4 kJ/mol and 78.5 kJ/mol at 40 wt%. The relationship between activation energy and KOH concentration is shown in Figure 9.

AlN activation energy values reported in the literature are mostly given for *c*-plane AlN.[18,19,25,35] They range from 8.4 kJ/mol to 64.7 kJ/mol depending on the crystalline quality of the AlN. We found one study reporting an activation energy of 114 kJ/mol for the etching of high-quality *a*-plane AlN grown on sapphire using AZ400K solution, a KOH-based developer containing approximately 2 wt% of KOH.[36]

The value of 100 kJ/mol reported in the present article for 5 wt% KOH is quite consistent with their findings given that higher KOH concentration leads to lower activation energy.

Note that the etching of nonpolar planes under heated KOH can only be observed on AlN. This is because the GaN/SiO_2 selectivity is less than one, causing the protective HM to erode faster than the GaN itself (see Figure S4).

DISCUSSIONS:

WET ETCHING PROPAGATION AND ROUGHNESS FORMATION:

In our previous work[12,17], we demonstrated how to produce straight III-N pillars using KOH etching and highlighted the difference in roughness formation between *a*- and *m*-oriented HM, but without a clear insight of the underlying mechanisms. This study allows us to gain deeper insight into how the wet etching process propagates, enabling us to explain the formation of straight pillars when the HM is present, as well as the origin of the roughness differences observed when using either an *a*- or *m*-oriented HM.

Consistently with the EBI parameter, defined by Lai et al,[26] *c*- and *m*- planes are the least vulnerable to KOH etching, and according to our observations these planes are stables at room temperatures. This explains why the wet etching propagation leads to the formation of staircase-like sidewalls composed of these stable *c*- and *m*-planes (see Equation 1). Another important point is the key role played by the HM. As mentioned earlier, keeping the HM in place shields the vulnerable top area from KOH etching,[12,28] preventing any chemical attack beneath the HM. The combination of EBI and HM protection provides a clear explanation for the observed anisotropic etching transfer in both 44 wt% and 5 wt% KOH concentrations (cf. Figure 5).

However, the EBI model alone is not sufficient to fully explain our results. Indeed, the wet etching progresses on our staircase pillars even though the *c*- and *m*- planes are stable. This indicates that the etching must occur elsewhere. To account for this propagation, we propose that KOH etching takes place at the kink locations, meaning at the intersection between the crystallographic planes. Three types of kink sites can be identified (cf. Figure 10a): *c*-/*m*-, *m*-/*m*-, and *c*-/*m*-/*m*- kinks. The observed progression of wet etching suggests that at least one of these kink sites is vulnerable to KOH. The vertical etching only stops once the bottom of the pillar is reached. Horizontal propagation can continue until the entire pillar is consumed. However, when a HM is present, it protects the vulnerable kink sites beneath it, halting the horizontal etching.

When a *m*-oriented HM is used, the wet etch propagates with *m*-planes parallel to the HM edges. (cf. Figure 10b). The sidewalls revealed by the wet treatment are mostly composed of a single or a few *m*-planes aligned with the HM edge, and the kink sites present at the pillar tops correspond to *c*-/*m*- kinks. After plasma patterning the HM sidewalls are rough and striated meaning that at the nanometer scale, the pillar top is not uniformly protected by the HM during the wet step. The absence of III-N etching locally at the pillar top edges demonstrates that the *c*-/*m*- kinks are robust to KOH etching. This robustness prevents the transfer of striations and

explains the smooth sidewalls observed on *m*-oriented pillars, as shown in Figure 6d and Figure 6j.

If a *a*-oriented HM is used, the pillar sidewalls are composed of multiple *m*-planes forming triangular prisms arranged in zig-zag and following the *a*-direction of the HM edges (cf. Figure 10c). This implies that pillars with *a*-oriented HM do not possess *a*-sidewalls after the KOH etching step. In this configuration, two kink sites are present at the top of the pillars: *c*-/*m*- kinks at the zig-zag edges and *c*-/*m*-/*m*- kinks at the zig-zag vertices. As observed in section 3.2, in this case, the HM striations are effectively transferred (suggesting that the pillar top is etched on areas not protected by the HM), indicating that one of the two types of kinks must be vulnerable to KOH etching. Since *m*-oriented HM shows that *c*-/*m*- kinks are stable, this suggests that *c*-/*m*-/*m*- kinks are the ones vulnerable to KOH etching

The *c*-/*m*-/*m*- kinks vulnerability to KOH explains the formation of rough sidewalls via the HM striation transfer with *a*-oriented HM, while the *c*-/*m*- kinks stability ensures the smooth sidewalls obtained with *m*-oriented HM.

These conclusions bring new insights on the sidewall's roughness formed during KOH wet etching according to the sidewall's orientation. Indeed, all the works that observed rougher *a*-planes than *m*-planes after KOH wet just concluded that *a*-planes were intrinsically rougher than *m*-planes.[15,23,27–29,37] However, that's not exactly the reason, as demonstrated above. The roughness generated according to the crystalline orientation is linked to the etching propagation mechanism (which takes place through the formation of *c* and *m* planes) combined with the presence of striations on the hard mask. KOH reveals smooth *m*-oriented sidewalls because they mostly consist of singular *m*-planes that do not replicate HM striations, while *a*-oriented surfaces are rougher due to the presence of multiple *m*-planes arranged in a zig-zag pattern that closely follow every HM defect.

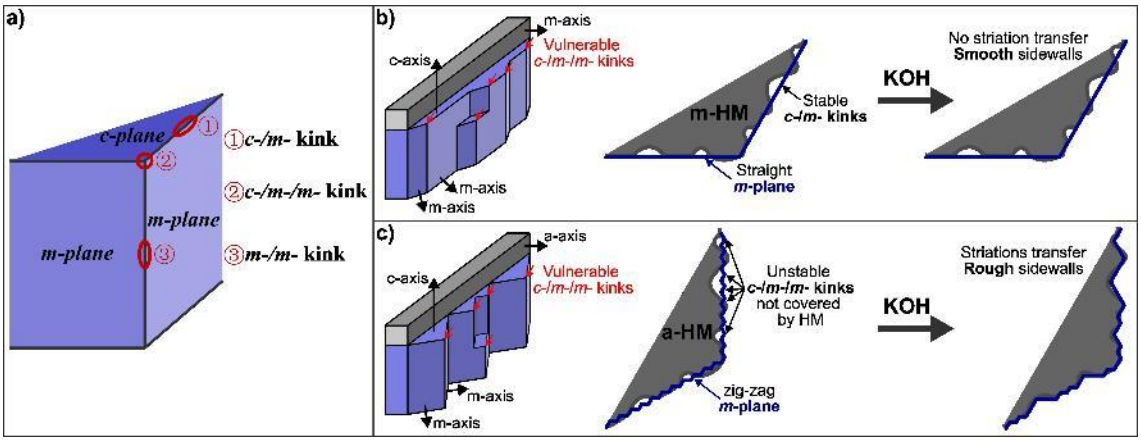

Figure 10. Illustration of: a) the crystallographic planes and kinks involved in the III-N wet etching process. Wet etching mechanisms leading to: b) smooth sidewalls when *m*-oriented HM is used; c) rough sidewalls when *a*-oriented HM is used. Adapted with permission from[17]. Copyright (2025) Elsevier.

IMPACT OF THE KOH CONCENTRATION AND TEMPERATURE SOLUTION:

For GaN, the KOH concentration appears to have minimal impact on the etching mechanisms, besides a slower etching rate at low concentrations. Pillars with both HM orientations look similar and no star-like shape has been observed. The only notable difference is the impossibility of obtaining vertical GaN pillars with 5 wt% KOH due to the HM erosion induced by such a long process time, making 44 wt% KOH the most suitable treatment.

However, we show that the etching of AlN is influenced by the KOH concentration. The transitory etching is different, with a symmetric staircase pattern for 44 wt% KOH (Figure 3b to Figure 3e), and a star-like shape for 5 wt% KOH (Figure 3g to Figure 3j). Moreover, Figure 3k reveals that under extended KOH duration, the intersection between two vertical planes is consumed with 5 wt% KOH while it remains stable with 44 wt% KOH. This suggests that the *m*-/*m*- kink sites do not have the same stability according to the KOH concentration used, and this may explain the different pattern (symmetric staircase vs star shape) formed during the wet progression with 5 wt% or 44 wt% KOH.

This vulnerability of the *m*-/*m*- kinks at low KOH concentrations and room temperature has been demonstrated by subjecting pillars to extended etching times (cf. Figure 11), which reveals a gradual etching of the sidewall corners, ultimately leading to the formation of a star-like shape. Note that such long exposure under 44 wt% KOH at room temperature does not lead to any sidewall etching due to the stability of the *m*-nonpolar planes.

Additionally, it can also explain why local and global roughness for *m*-oriented HM is lower with 5 wt% KOH than with 44 wt% KOH. Indeed, the misalignment between the AlN crystallographic plane and the lithography pattern is hard to avoid. This is why we have observed in the previous section some jumps and steps on the sidewalls (cf. Figure 6b and Figure 6k). In the case of 5 wt% KOH, those steps are less numerous or less high. This is because they are progressively etched away through the *m*-/*m*- kinks, resulting in significantly smoother sidewalls when treated with 5 wt% KOH compared to 44 wt%. However, this smoothing comes at the expense of the hexagonal corners, which are blunted and lose their sharpness.

We suspect that this different wet etching propagation with concentration may be attributed to the K^+ cations. Indeed, by increasing the KOH concentration both the concentration of the OH^- anionic reactant and K^+ cation are increased. The cation concentration can affect the etch propagation by physically or chemically blocking some sites.[38] We think that the increased presence of K^+ cations at high KOH concentrations lead to their accumulation on the pillar sidewalls (as evidenced by the EDX analysis presented in Figure S5), preventing the etching of the *m*-/*m*- sites.

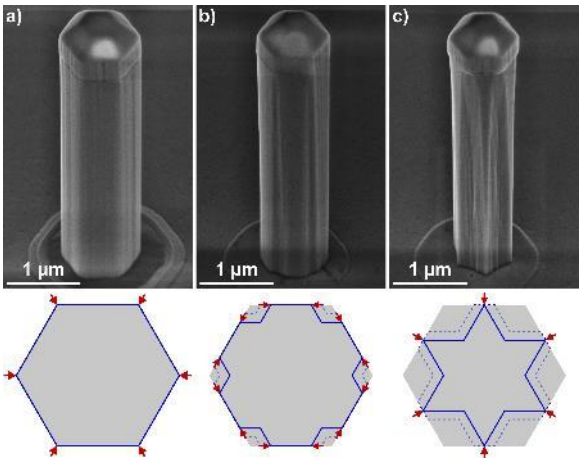

Figure 11. Evolution of AlN pillars under extended 5 wt% KOH treatments at room temperature during a) 30 min, b) 4 hours, c) 16 hours. The top section displays the AlN pillars, while the bottom section illustrates the etching progression (red arrows) through the *m*-/*m*-kinks.

SUMMARY AND CONCLUSION:

In this article, we investigate the mechanisms involved during KOH wet etching applied on AlN and GaN pillars previously obtained by Cl_2 plasma etching and with a hexagonal hard mask whose edges are oriented either with *a*- or *m*-nonpolar III-N crystallographic orientation.

We discuss the impact of the KOH concentration and the solution temperature on the etching kinetics, the etch propagation mechanisms, the crystallographic plane stability, and the roughness formation.

AlN and GaN present almost the same wet etching behavior except that GaN is etched 30 to 60 times slower. Both an increase of the KOH concentration or the solution temperature lead to an increase of the etch rate. The etch follows an Arrhenius law with temperature. From the tapered sidewalls (composed of several semipolar planes) present after plasma patterning, the wet etch propagates laterally and vertically through the formation of successive *c*- and *m*-planes which are the most stable under KOH. The vertical etch propagation is about 20 times higher than the lateral one. Moreover, the presence of an HM prevents the lateral erosion at the top of

the pillars directing the wet etch to propagate predominantly vertically. This allows an anisotropic transfer of the HM shape and dimension. Thus, if a *m*- (and resp. *a*-) oriented HM is used, III-N pillars with *m*- (and resp. *a*-) oriented sidewalls are obtained. However, in the case of *a*-oriented HM, the pillar sidewalls are aligned with *a*-crystallographic planes at the microscopic scale but at the nanometer scale, the sidewalls are composed of successive *m*-planes following the *a*-orientation.

We highlight that the wet etch mainly occurs at some kink sites present at the intersection between the *c* and *m* crystallographic planes. Three types of kink sites are identified: *c*-/*m*-, *m*-/*m*-, and *c*-/*m*-/*m*-. The vulnerability of those three kink sites according to the KOH concentration and temperature (summarized in Table 2) drives the wet etch propagation and explains the roughness formation observed in this study.

Regarding the vertical etch propagation, we show that the *c*-/*m*-/*m*- kink sites are vulnerable to KOH etch while the *c*-/*m*- ones are stables. Thus, if a *a*-oriented HM is used during wet KOH, the *c*-/*m*-/*m*- kink sites present at the pillar top and not protected by the hard mask are attacked. The etching progression halts once all the unprotected III-N top areas are removed, i.e., when the lateral etching reaches the hard mask. Consequently, the nanometer scale striated roughness of the HM sidewalls is faithfully transferred into the III-N sidewalls, resulting in striated *a*-oriented sidewalls. On the other hand, if a *m*-oriented HM is used, the *c*-/*m*- kink sites at the pillar top not protected by the HM are robust enough to KOH to not be attacked and to avoid the HM striation transfer, thus allowing the obtaining of smooth *m*-oriented sidewalls.

This trend is true whatever the KOH concentration, the solution temperature, and the III-N (GaN or AlN).

Regarding the lateral etch propagation, we show that in the case of AlN, *m*-/*m*- kink sites are less stable at 5 wt% KOH than at 44 wt% KOH for any temperatures. This fact explains why the wet etch propagates with star-like patterns at 5 wt% KOH instead of staircase-like patterns

at 44 wt%. We attribute this effect to the K^+ cations that are assumed to be particularly attracted to *m*-/*m*- kink sites preventing their attack. However, for both concentrations, the final result is similar and conducts to an anisotropic transfer of the HM shape and dimensions.

Finally, the *m*-nonpolar plane seems extremely stable at room temperature, allowing some extended etch time without lateral etching of the nonpolar plane (if no *m*-/*m*- kink sites in the case of low KOH concentration). In contrast, with hot KOH, once the HM is anisotropically transferred, the lateral etching of the nonpolar vertical planes can occur. This ability of heated KOH to etch nonpolar planes could potentially be utilized to controllably reduce the pillar diameter below a hundred nanometers, allowing the fabrication of nanopillars with ultra-high aspect ratio superior to 40 (cf. Figure 8h).

Table 2. Robustness of the different planes/kinks to 5 wt% and 44 wt% KOH at low (20°C) and high (60-80°C) temperature.

	Low T°		High T°	
	5%	44%	5%	44%
c-plane	++	++	++ (?)	++ (?)
Nonpolar planes	++	++	+	+
Semipolar planes	-	-	--	--
c-/*m*- kinks	++	++	++	++
c-/*m*-/*m*- kinks	-	-	--	--
m-/*m*- kinks	+	++	+	+

With ++: Robust, no etching observed. +: mostly robust, etching only for extended times. -: Vulnerable, fast etching. --: Vulnerable, very fast etching. (?): Assumed, no direct measurement.

This study highlights the significant benefits of combining plasma etching and wet etching to fabricate straight, smooth, and *m*-faceted III-N nanostructures. For both GaN and AlN, a plasma

etching step producing slightly tapered pillars is mandatory to ensure the HM shape transfer during the following step. For the KOH wet etching, utilizing a heated solution (60°C to 80°C) allows for reasonable process times. For AlN, 5 wt% KOH is preferred as it tends to produce smoother sidewalls, while for GaN, higher KOH concentrations are necessary to achieve straight and smooth profiles. This two-step process proves its efficiency to fabricate high aspect ratio AlN and GaN pillars with smooth and *m*-facetted sidewalls that can be used as a building block for the fabrication of eco-friendly energy-efficient UV sources in a core-shell architecture.

AUTHOR INFORMATION

Corresponding Author

Email: erwine.pargon@cea.fr

Author Contributions

Jaloustre Lucas: Conducted the conceptualization, methodology, investigation, data curation, validation, and writing (original draft and review). Sales De Mello Saron: Contributedto the review process. Labau Sébastien: Responsible for the lithography process. Petit-Etienne Camille: Is in charge of the supervision, and participate to the review. Pargon Erwine: Initiate and supervised the project, manage funding acquisition, and contributed to the conceptualization and writing (original draft and review).

Supporting Information

Titration of OH- concentration in room temperature and heated KOH solutions; AFM surface profiles of GaN pillars; Heated KOH: additional concentrations; Heated KOH on GaN; Potassium accumulation under high KOH concentration: EDX analysis.

Acknowledgments

The authors would like to thank Joelle El Hayek and Jean-Hervé Tortai for their valuable advice, assistance, and prompt support in setting up the titration experiments.

Funding Sources

This research was funded by the French National Research Agency in the framework of the program ANR-22-CE51-0032-01 and the French National Research Agency in the framework of the "Investissements d'avenir" program (ANR-15-IDEX-02). It was also supported by the French RENATECH network.

ABBREVIATIONS

UV, ultra-violet; LED, light emitting diode; TMAH, tetramethylammonium hydroxide; EBI, etching barrier index; HM, hard mask; PECVD, plasma enhanced chemical vapor deposition; TEOS, tetraethoxysilane; CW, carrier wafer; MERIE, magnetically enhanced reactive ion etching; ICP, inductively coupled plasma; DPS, decoupled plasma source; HF, hydrofluoric acid; SEM, scanning electron microscope; AFM, atomic force microscope; FIB, focused ion beam; RMS, root mean square; ER, etching rate.

REFERENCES

(1) Zhou, C.; Ghods, A.; Saravade, V. G.; Patel, P. V.; Yunghans, K. L.; Ferguson, C.; Feng, Y.; Kucukgok, B.; Lu, N.; Ferguson, I. T. Review—The Current and Emerging Applications of the III-Nitrides. *ECS J. Solid State Sci. Technol.* **2017**, *6* (12), Q149–Q156. https://doi.org/10.1149/2.0101712jss.

(2) Fan, X.; Shi, J.; Chen, Y.; Miao, G.; Jiang, H.; Song, H. A Comprehensive Review of Group-III Nitride Light-Emitting Diodes: From Millimeter to Micro-Nanometer Scales. *Micromachines* **2024**, *15* (10), 1188. https://doi.org/10.3390/mi15101188.

(3) Kneissl, M.; Seong, T.-Y.; Han, J.; Amano, H. The Emergence and Prospects of Deep-Ultraviolet Light-Emitting Diode Technologies. *Nat. Photonics* **2019**, *13* (4), 233–244. https://doi.org/10.1038/s41566-019-0359-9.

(4) Valera, L.; Jaloustre, L.; Reita, V.; De Mello, S. R. S.; Bellet-Amalric, E.; Petit-Étienne, C.; Pargon, E.; Jacopin, G.; Durand, C. Organized AlN Nanowire Arrays by Hybrid Approach of Top-Down Processing and MOVPE Overgrowth for Deep UV Emission Devices. *ACS Appl. Nano Mater.* **2024**, *7* (9), 10338–10349. https://doi.org/10.1021/acsanm.4c00814.

(5) Le Boulbar, E. D.; Lewins, C. J.; Allsopp, D. W. E.; Bowen, C. R.; Shields, P. A. Fabrication of High-Aspect Ratio GaN Nanostructures for Advanced Photonic Devices.

Microelectronic Engineering **2016**, *153*, 132–136. https://doi.org/10.1016/j.mee.2016.03.058.
(6) Coulon, P.-M.; Feng, P.; Wang, T.; Shields, P. Impact of Inductively Coupled Plasma Etching Conditions on the Formation of Semi-Polar (11-22) and Non-Polar (11-20) GaN Nanorods. *Nanomaterials* **2020**, *10* (12), 2562. https://doi.org/10.3390/nano10122562.
(7) Frye, C. D.; Reinhardt, C. E.; Donald, S. B.; Voss, L. F.; Harrison, S. E. ICP Etching of GaN Microstructures in a Cl_2–Ar Plasma with Subnanometer-Scale Sidewall Surface Roughness. *Materials Science in Semiconductor Processing* **2022**, *144*, 106564. https://doi.org/10.1016/j.mssp.2022.106564.
(8) Tahhan, M.; Nedy, J.; Chan, S. H.; Lund, C.; Li, H.; Gupta, G.; Keller, S.; Mishra, U. Optimization of a Chlorine-Based Deep Vertical Etch of GaN Demonstrating Low Damage and Low Roughness. *Journal of Vacuum Science & Technology A: Vacuum, Surfaces, and Films* **2016**, *34* (3), 031303. https://doi.org/10.1116/1.4944054.
(9) Rawal, D. S.; Arora, H.; Sehgal, B. K.; Muralidharan, R. Comparative Study of GaN Mesa Etch Characteristics in Cl_2 Based Inductively Coupled Plasma with Ar and BCl_3 as Additive Gases. *Journal of Vacuum Science & Technology A: Vacuum, Surfaces, and Films* **2014**, *32* (3), 031301. https://doi.org/10.1116/1.4868616.
(10) Smith, S. A.; Wolden, C. A.; Bremser, M. D.; Hanser, A. D.; Davis, R. F.; Lampert, W. V. High Rate and Selective Etching of GaN, AlGaN, and AlN Using an Inductively Coupled Plasma. *Appl. Phys. Lett.* **1997**, *71* (25), 3631–3633. https://doi.org/10.1063/1.120463.
(11) Jaloustre, L.; Ackermann, V.; Mello, S. S. D.; Labau, S.; Petit-Etienne, C.; Pargon, E. Preferential Crystal Orientation Etching of GaN Nanopillars in Cl2 Plasma. *Materials Science in Semiconductor Processing* **2023**, *165*, 107654. https://doi.org/10.1016/j.mssp.2023.107654.
(12) Jaloustre, L.; Sales De Mello, S.; Labau, S.; Petit-Etienne, C.; Pargon, E. Fabrication of High Aspect Ratio AlN Nanopillars by Top-down Approach Combining Plasma Etching and Wet Etching. *Materials Science in Semiconductor Processing* **2024**, *181*, 108615. https://doi.org/10.1016/j.mssp.2024.108615.
(13) Coulon, P.-M.; Kusch, G.; Fletcher, P.; Chausse, P.; Martin, R.; Shields, P. Hybrid Top-Down/Bottom-Up Fabrication of a Highly Uniform and Organized Faceted AlN Nanorod Scaffold. *Materials* **2018**, *11* (7), 1140. https://doi.org/10.3390/ma11071140.
(14) Coulon, P.-M.; Kusch, G.; Martin, R. W.; Shields, P. A. Deep UV Emission from Highly Ordered AlGaN/AlN Core–Shell Nanorods. *ACS Appl. Mater. Interfaces* **2018**, *10* (39), 33441–33449. https://doi.org/10.1021/acsami.8b10605.
(15) Dannecker, K.; Baringhaus, J. Fabrication of Crystal Plane Oriented Trenches in Gallium Nitride Using SF6 + Ar Dry Etching and Wet Etching Post-Treatment. *Journal of Vacuum Science & Technology A: Vacuum, Surfaces, and Films* **2020**, *38* (4), 043204. https://doi.org/10.1116/6.0000120.
(16) Guo, W.; Xie, J.; Akouala, C.; Mita, S.; Rice, A.; Tweedie, J.; Bryan, I.; Collazo, R.; Sitar, Z. Comparative Study of Etching High Crystalline Quality AlN and GaN. *Journal of Crystal Growth* **2013**, *366*, 20–25. https://doi.org/10.1016/j.jcrysgro.2012.12.141.
(17) Jaloustre, L.; Mello, S. S. D.; Labau, S.; Petit-Etienne, C.; Pargon, E. Faceting Mechanisms of GaN Nanopillar under KOH Wet Etching. *Materials Science in Semiconductor Processing* **2024**, *173*, 108095. https://doi.org/10.1016/j.mssp.2023.108095.
(18) Mileham, J. R.; Pearton, S. J.; Abernathy, C. R.; MacKenzie, J. D.; Shul, R. J.; Kilcoyne, S. P. Wet Chemical Etching of AlN. *Applied Physics Letters* **1995**, *67* (8), 1119–1121. https://doi.org/10.1063/1.114980.

(19) Mileham, J. R.; Pearton, S. J.; Abernathy, C. R.; MacKenzie, J. D.; Shul, R. J.; Kilcoyne, S. P. Patterning of AlN, InN, and GaN in KOH-Based Solutions. *Journal of Vacuum Science & Technology A: Vacuum, Surfaces, and Films* **1996**, *14* (3), 836–839. https://doi.org/10.1116/1.580399.
(20) Behzadirad, M.; Nami, M.; Wostbrock, N.; Zamani Kouhpanji, M. R.; Feezell, D. F.; Brueck, S. R. J.; Busani, T. Scalable Top-Down Approach Tailored by Interferometric Lithography to Achieve Large-Area Single-Mode GaN Nanowire Laser Arrays on Sapphire Substrate. *ACS Nano* **2018**, *12* (3), 2373–2380. https://doi.org/10.1021/acsnano.7b07653.
(21) Coulon, P.; Kusch, G.; Le Boulbar, E. D.; Chausse, P.; Bryce, C.; Martin, R. W.; Shields, P. A. Hybrid Top-Down/Bottom-Up Fabrication of Regular Arrays of AlN Nanorods for Deep-UV Core–Shell LEDs. *Physica Status Solidi (b)* **2018**, *255* (5), 1700445. https://doi.org/10.1002/pssb.201700445.
(22) Debnath, R.; Ha, J.-Y.; Wen, B.; Paramanik, D.; Motayed, A.; King, M. R.; Davydov, A. V. Top-down Fabrication of Large-Area GaN Micro- and Nanopillars. *Journal of Vacuum Science & Technology B, Nanotechnology and Microelectronics: Materials, Processing, Measurement, and Phenomena* **2014**, *32* (2), 021204. https://doi.org/10.1116/1.4865908.
(23) Itoh, M.; Kinoshita, T.; Koike, C.; Takeuchi, M.; Kawasaki, K.; Aoyagi, Y. Straight and Smooth Etching of GaN (1-100) Plane by Combination of Reactive Ion Etching and KOH Wet Etching Techniques. *Jpn. J. Appl. Phys.* **2006**, *45* (5A), 3988–3991. https://doi.org/10.1143/JJAP.45.3988.
(24) Kazanowska, B. A.; Sapkota, K. R.; Lu, P.; Talin, A. A.; Bussmann, E.; Ohta, T.; Gunning, B. P.; Jones, K. S.; Wang, G. T. Fabrication and Field Emission Properties of Vertical, Tapered GaN Nanowires Etched via Phosphoric Acid. *Nanotechnology* **2022**, *33* (3), 035301. https://doi.org/10.1088/1361-6528/ac2981.
(25) Guo, W.; Kirste, R.; Bryan, I.; Bryan, Z.; Hussey, L.; Reddy, P.; Tweedie, J.; Collazo, R.; Sitar, Z. KOH Based Selective Wet Chemical Etching of AlN, AlxGa1−xN, and GaN Crystals: A Way towards Substrate Removal in Deep Ultraviolet-Light Emitting Diode. *Applied Physics Letters* **2015**, *106* (8), 082110. https://doi.org/10.1063/1.4913705.
(26) Lai, Y.-Y.; Hsu, S.-C.; Chang, H.-S.; Wu, Y. S.; Chen, C.-H.; Chen, L.-Y.; Cheng, Y.-J. The Study of Wet Etching on GaN Surface by Potassium Hydroxide Solution. *Research on Chemical Intermediates* **2017**, *43* (6), 3563–3572. https://doi.org/10.1007/s11164-016-2430-1.
(27) Liu, G.; Wen, B.; Xie, T.; Castillo, A.; Ha, J.-Y.; Sullivan, N.; Debnath, R.; Davydov, A.; Peckerar, M.; Motayed, A. Top–down Fabrication of Horizontally-Aligned Gallium Nitride Nanowire Arrays for Sensor Development. *Microelectronic Engineering* **2015**, *142*, 58–63. https://doi.org/10.1016/j.mee.2015.08.004.
(28) He, J.; Feng, M.; Zhong, Y.; Wang, J.; Zhou, R.; Gao, H.; Zhou, Y.; Sun, Q.; Liu, J.; Huang, Y.; Zhang, S.; Wang, H.; Ikeda, M.; Yang, H. On-Wafer Fabrication of Cavity Mirrors for InGaN-Based Laser Diode Grown on Si. *Sci Rep* **2018**, *8* (1), 7922. https://doi.org/10.1038/s41598-018-26305-8.
(29) Al Taradeh, N.; Frayssinet, E.; Rodriguez, C.; Morancho, F.; Sonneville, C.; Phung, L.-V.; Soltani, A.; Tendille, F.; Cordier, Y.; Maher, H. Characterization of M-GaN and a-GaN Crystallographic Planes after Being Chemically Etched in TMAH Solution. *Energies* **2021**, *14* (14), 4241. https://doi.org/10.3390/en14144241.
(30) Yu, F.; Yao, S.; Römer, F.; Witzigmann, B.; Schimpke, T.; Strassburg, M.; Bakin, A.; Schumacher, H. W.; Peiner, E.; Wasisto, H. S.; Waag, A. GaN Nanowire Arrays with Nonpolar Sidewalls for Vertically Integrated Field-Effect Transistors. *Nanotechnology* **2017**, *28* (9), 095206. https://doi.org/10.1088/1361-6528/aa57b6.

(31) Li, D.; Sumiya, M.; Fuke, S.; Yang, D.; Que, D.; Suzuki, Y.; Fukuda, Y. Selective Etching of GaN Polar Surface in Potassium Hydroxide Solution Studied by X-Ray Photoelectron Spectroscopy. *Journal of Applied Physics* **2001**, *90* (8), 4219–4223. https://doi.org/10.1063/1.1402966.
(32) Seidel, H.; Csepregi, L.; Heuberger, A.; Baumgärtel, H. Anisotropic Etching of Crystalline Silicon in Alkaline Solutions: I . Orientation Dependence and Behavior of Passivation Layers. *J. Electrochem. Soc.* **1990**, *137* (11), 3612–3626. https://doi.org/10.1149/1.2086277.
(33) Zhuang, D.; Herro, Z. G.; Li, X.; Schlesser, R.; Sitar, Z. Wet Etching of Bulk AlN Crystals. *MRS Proc.* **2006**, *955*, 0955-I07-10. https://doi.org/10.1557/PROC-0955-I07-10.
(34) Palacios, T.; Calle, F.; Varela, M.; Ballesteros, C.; Monroy, E.; Naranjo, F. B.; Sánchez-García, M. A.; Calleja, E.; Muñoz, E. Wet Etching of GaN Grown by Molecular Beam Epitaxy on Si(111). *Semicond. Sci. Technol.* **2000**, *15* (10), 996–1000. https://doi.org/10.1088/0268-1242/15/10/312.
(35) Vartuli, C. B.; Pearton, S. J.; Lee, J. W.; Abernathy, C. R.; Mackenzie, J. D.; Zolper, J. C.; Shul, R. J.; Ren, F. Wet Chemical Etching of AlN and InAlN in KOH Solutions. *J. Electrochem. Soc.* **1996**, *143* (11), 3681–3684. https://doi.org/10.1149/1.1837271.
(36) Kazanowska, B. A. Chemical Wet Etching of $Al_{(x)}Ga_{(1-x)}N_{(0\leq x\leq 1)}$ Nanostructures, University of Florida, 2021.
(37) Baik, K. H.; Song, H.-Y.; Hwang, S.-M.; Jung, Y.; Ahn, J.; Kim, J. Etched Surface Morphology of Heteroepitaxial Nonpolar (11-20) and Semipolar (11-22) GaN Films by Photoenhanced Chemical Wet Etching. *J. Electrochem. Soc.* **2011**, *158* (4), D196–D199. https://doi.org/10.1149/1.3544916.
(38) Gosálvez, M. A.; Sato, K.; Foster, A. S.; Nieminen, R. M.; Tanaka, H. An Atomistic Introduction to Anisotropic Etching. *J. Micromech. Microeng.* **2007**, *17* (4), S1–S26. https://doi.org/10.1088/0960-1317/17/4/S01.